Visualizing Current in Superconducting Networks

X. Wang,[1,2] M. Laav,[1,2,3] I. Volotsenko,[1,2,3] A. Frydman,[1,2,3] and B. Kalisky[1,2,*]

[1] *Department of Physics, Bar-Ilan University, Ramat Gan 5290002, Israel*

[2] *Institute of Nanotechnology and Advanced Materials, Bar-Ilan University, Ramat Gan 5290002, Israel*

[3] *Jack and Pearl Resnick Institute, Bar-Ilan University, Ramat Gan 5290002, Israel*

(Received 29 July 2021; revised 20 October 2021; accepted 31 January 2022; published 28 February 2022)

We present an experimental study of local magnetic imaging in order to visualize the current flow in superconducting networks. We track the evolution of the spatial distribution of the current flow as the network is driven from fully superconducting to fully normal phases. Our results highlight the factors that contribute to the disordered flow in superconducting networks during their collapse, and demonstrate that the current is never uniformly distributed in the network. These results can assist the design and development of circuits based on superconductors and Josephson junctions.

DOI: 10.1103/PhysRevApplied.17.024073

I. INTRODUCTION

Superconducting networks have become an element in the development of quantum-information circuits [1]. These can be arrays of Josephson junctions, weak superconducting links, or superconducting wires, which may act as qbits or readouts [2–5]. This development calls for diagnostic tools to detect elements that are faulty or cause unwanted behavior. Several imaging techniques have been successfully applied to diagnose integrated circuits [6–8]. For circuits that include superconducting elements, it is desirable to map not only the current flow or the heat source, but also the superconductivity itself.

Theoretically, current flow in disordered media can be treated as a random resistor network (RRN). When dealing with a disordered superconductor, additional considerations need to be taken into account such as critical currents and temperatures, which dynamically alter the conduction map of the superconducting RRN [9–13]. The same treatment has been traditionally applied to Josephson-junction arrays and superconducting networks [14–17]. However, a useful factor in determining the actual flow of currents in superconducting circuits and arrays is the Meissner effect. This effect, which shields a superconductor from magnetic fields by counter supercurrents at the sample edges, is typically ignored.

In this work we study the current flow in superconducting networks by noninvasive mapping the local current. We show that the current distribution depends on the proximity of the system to the superconducting transition. Deep in the superconducting phase the flow is concentrated mainly at the edges due to Meissner screening, independent of the way the current is injected to the system. Close to criticality, on the other hand, superconducting inhomogeneity governs the current flow and overshadows the influence of the Meissner effect. In addition, the current pattern is very sensitive to the precise way current is driven into the network.

II. EXPERIMENTAL DETAILS

To model an inhomogeneous superconductor, we prepare a set of 50-nm-thick Nb superconducting networks with $T_c = 8.5$ K (S1–S4) on glass (S1) or Silicon (S2–S4) substrates. The Nb is deposited by e-beam evaporation under UHV conditions. The networks are fabricated by standard photolithography and lift-off procedures using a Heidelberg-instruments MLA 150 system. We use two networks' geometries: (i) 720×720 μm^2 networks composed of 20×4 μm^2 segments (S1 and S4, the dimension of the segments is represented as L), and (ii) 310×310 μm^2 networks composed of 10×2 μm^2 segments (S2 and S3). The networks were connected to large continuous pads of either Nb (S1, S2, and S3) or Au (S4). See Figs. 1(a) and 3(a).

To spatially map the distribution of the current flow, noninvasively, we map the magnetic fields generated by the current flow. Magnetic imaging on the microscale can be performed by several techniques, such as magneto-optics, magnetic force microscopy, scanning Hall microscopy, scanning superconducting quantum interference device (SQUID), and more. Here, we choose to use scanning SQUID microscopy for two reasons. First, its high magnetic sensitivity, capable of detecting the fields generated by small amounts of current (down to 1 nA)

*beena@biu.ac.il

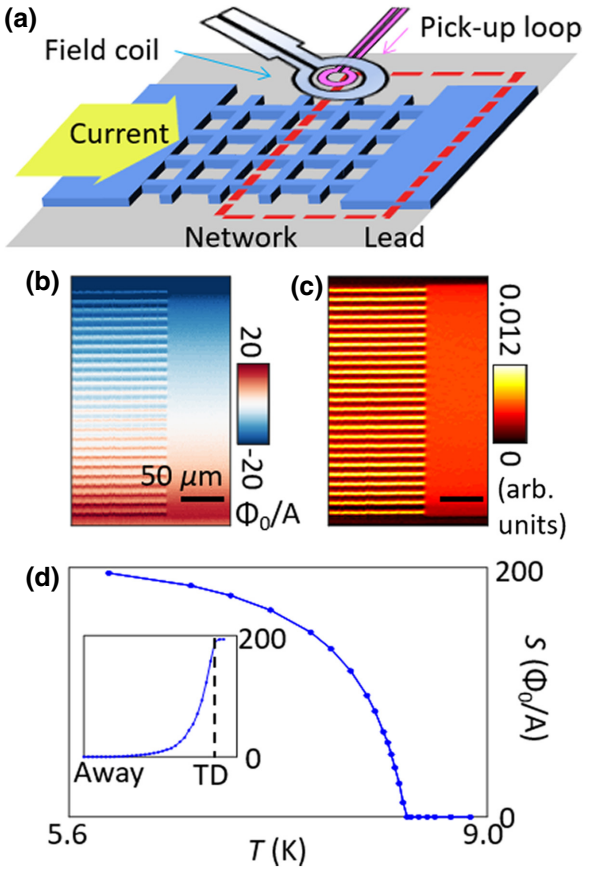

FIG. 1. (a) Illustration of scanning SQUID measurement over superconducting networks used in this study. The sensor captures field lines that are generated by current flowing in the sample. The outer loop, the field coil, applies a local magnetic field to measure susceptibility as a function of location. (b) Local flux map of S2, taken at 8.6 K (above T_c), of the area sketched in (a). (c) $|\vec{J}(x,y)|$ extracted from the data in (b). (d) The amplitude of diamagnetic response S as a function of the temperature T taken on the lead of sample S3, about 100 μm away from the grid. The diamagnetic signal disappears at T_c. Inset: susceptibility as a function of sensor-sample height. Touchdown position is marked by a dashed line.

[18–20]. Second, its ability to capture several properties simultaneously, which allows mapping the local diamagnetic response [21,22] in addition to imaging the current flow.

For imaging the flow of electric current we raster the sensor's pick-up loop over the sample and record the field lines that are generated by transport current flowing in the sample. To separate the flux generated by currents flowing in the sample from the dc SQUID signal, we use a lock-in technique with frequency up to several kHz. For this study we use relatively small currents, up to 1 mA. Applying higher current causes the resistance versus temperature curves to crossover from a continuous superconducting transition to an abrupt, hysteretic transition. This will be the subject of a future publication. We use Fourier analysis based on Biot-Savart's law to invert magnetic flux maps into current density maps $[\vec{J}(x,y) = J_x\vec{x} + J_y\vec{y}]$ [23,24]. This analysis takes into account the SQUID's point spread function, measured independently. Typical data and reconstructed current distribution maps are shown in Figs. 1(b) and 1(c). The plots show an absolute value of current density $|\vec{J}(x,y)| = \sqrt{J_x^2 + J_y^2}$.

In addition to mapping the current distribution, we simultaneously map the local susceptibility, yielding information about the strength of local superconductivity [21,22,25,26]. The sensor is composed of a concentric pick-up loop (inner sensing loop) and excitation field coil (outer loop), see Fig. 1(a). For magnetic susceptibility measurement, we apply local magnetic field using the field coil, and lock-in to the SQUID signal to record the diamagnetic response of the superconductor, in units of Φ_0/A [Fig. 1(d)] where Φ_0 is the flux quanta $\Phi_0 = h/2e$. Near a superconductor, susceptibility provides the diamagnetic response of the sample. Far away from the superconductor the sensor captures the field applied by the field coil. Near a superconductor the applied field is eliminated by the superconductor, therefore leading to reading decreases. The difference between these two readings is the diamagnetic signal of that location $[S(x,y)]$. The two measurements described here, current imaging and susceptibility maps, are measured by the SQUID as a response to an excitation, transport current in the first, and local magnetic field in the second. The basic dc SQUID measurement shows the static magnetic landscape, which includes Abrikosov vortices and trapped flux.

III. RESULTS

We begin by comparing the current flow in the superconducting and the normal states. Figure 2 shows the extracted current-density maps of sample S3 above and below T_c. The current is homogeneous in the normal state reflecting the uniformity of the sample. In the continuous superconducting region leading to the grid (denoted in this paper as the "lead") we observe the concentration of the currents near the edges of the sample as expected from shielding current due to the Meissner effect. This is less natural in the superconducting network since it is composed of individual superconducting sections and each should carry its own Meissner currents in addition to the overall Meissner screening of the interconnected object. Nevertheless, the profile of current distribution across the network is similar to that in the continuous pad. This is demonstrated in (f), where we bin the current distribution in the continuous superconducting region (the lead) into 25 sections, in order to compare it with the flow pattern in the grid. The extent of Meissner influence in the lead (black data) completely overlaps with the data measured for the grid (green).

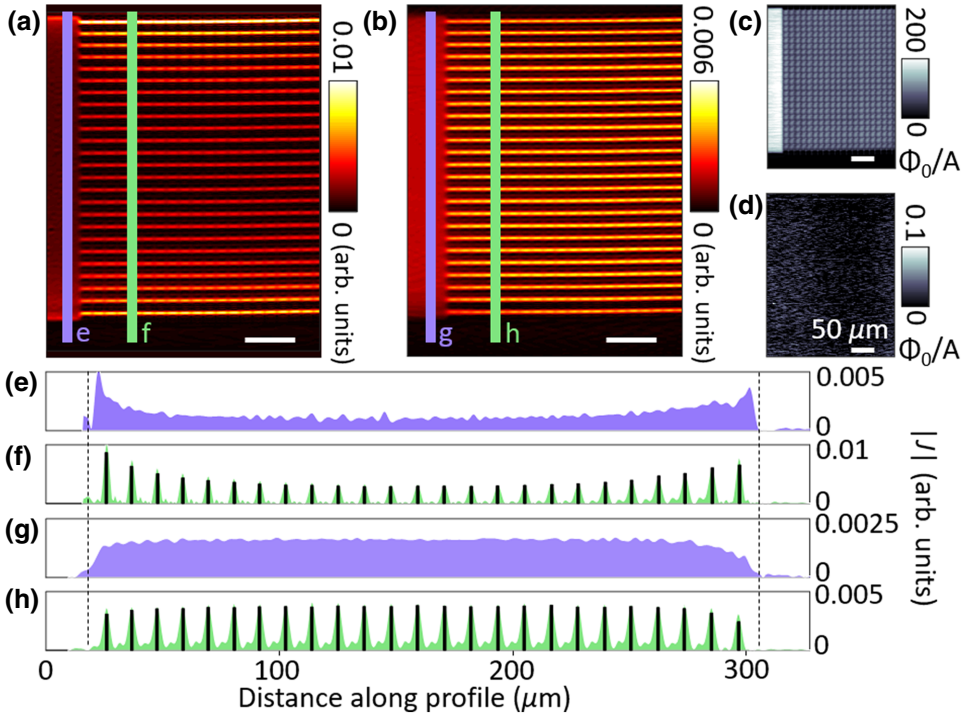

FIG. 2. $|\vec{J}(x,y)|$ maps at superconducting (6.4 K) (a) and normal (8.5 K) (b) states of S3. (c)–(d) Corresponding susceptibility images. While a strong diamagnetic response is observed in the superconducting state (c), no signal other than SQUID noise is recorded in the normal state (d). (e)–(h) Cross sections taken from the current density maps on the lead [purple, (e),(g)] and on the grid [green, (f),(h)] for both the superconducting (e),(f) and the normal (g),(h) states. The black bars in (f) and (g) are a result of binning the lead data to 25 sections, in order to compare the overall distribution of the current between the lead and the grid. A good resemblance is found between the black bars and the green peaks. All scale bars represent 50 μm.

Thus, despite the porous nature of the network, it maintains an overall shielding as if it was a continuous superconductor. This has significant implication on our understanding of current flow in ordered Josephson-junction arrays or superconducting networks, because even for a very homogeneous system, the current is carried only by a small fraction of the segments.

Note that in both the normal and superconducting phases the flow is mostly horizontal. In the resistive state, dissipative vertical flow is avoided, while in the superconductor, there is no preferable direction leading to average zero vertical flow.

One could suspect that the nonhomogeneous current distribution in the network (similar to that in the lead) is a consequence of current continuity. In other words, the current is injected mainly near the edges thus influencing the flow in the network. To test this we conduct a similar measurement on sample S4, which has normal Au leads. The results are shown in Fig. 3. Despite the homogeneous flow in the pad that injects the current evenly to the different network sections, the current in the network is concentrated at the edges. The rearrangement of currents requires vertical flow at the left and right edges of the grid (which is "cost free" for a superconductor). This vertical flow is clearly apparent in the current density map [Fig. 3(b)].

Such nonhomogeneous flow due to Meissner screening can be expected at all length scales, provided that the penetration depth λ is smaller than L. In this case the shielding currents will be focused on the edges of the grid, as observed in Fig. 2. On the other hand, if $\lambda > L$ the shielding currents extend over a large part of the grid, resulting in a more homogeneous flow. The dimensions of superconducting devices L in the literature range from 1 to 10 μm [1,3,27–30]. In this work we choose network link $L \sim 10$ μm in order to assure that $\lambda < L$ as close as possible to T_c.

The behavior presented above applies to networks that are deep in the superconducting phase, or completely normal. Near criticality, close to the superconducting

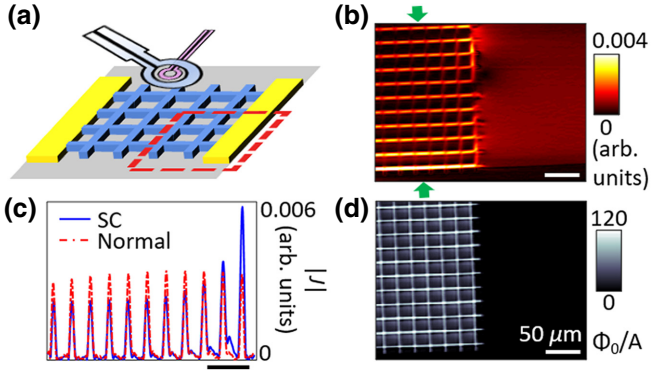

FIG. 3. (a) Sketch of the measurement on sample S4 having normal Au leads. The dashed line marks the scanned area. (b) $|\vec{J}(x,y)|$ at 4.4 K (superconducting state of the network). (c) Cross sections of the current density map of the network at the superconducting (4.4 K) and normal (8.9 K) states. The location of cross section is marked by green arrows in (b). (d) Susceptibility map of the same area, demonstrating a fully superconducting network and a normal lead.

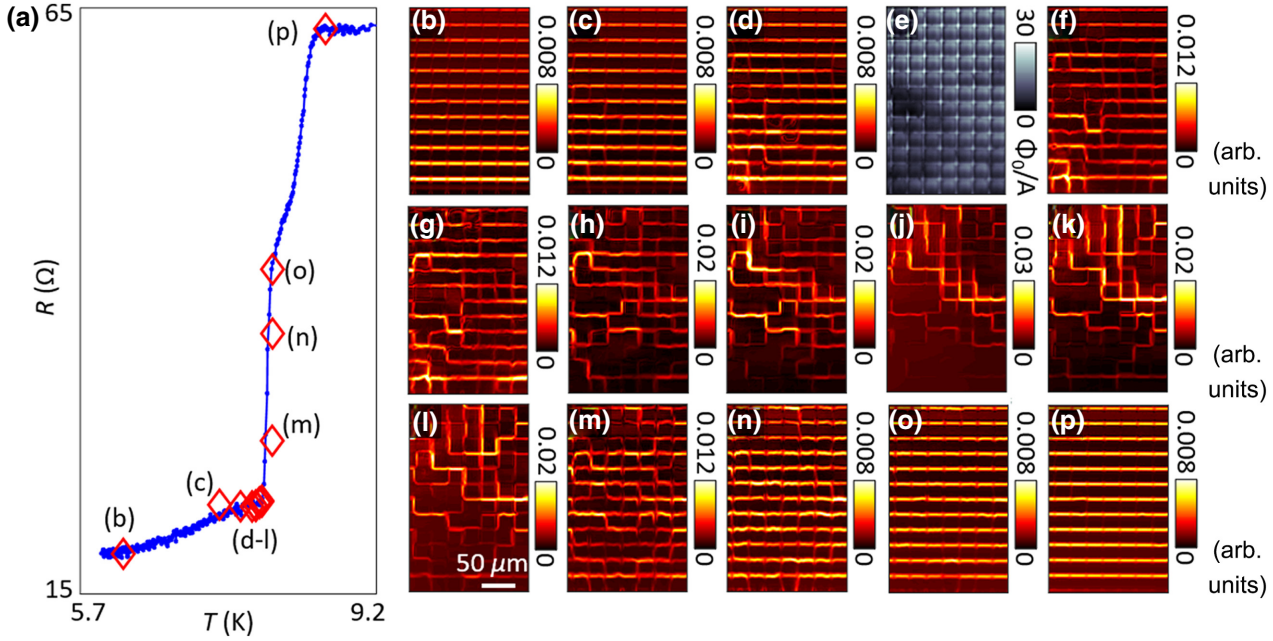

FIG. 4. (a) The resistance versus temperature curve (R versus T) of sample S1 (blue dots), together with relative positions of current density images [red rhomboids, (b)–(d) and (f)–(p)] as a function of temperature. (b)–(d), (f)–(p) $|\vec{J}(x,y)|$ maps of a small region, showing the full transition procedure from deep superconducting state (6.1 K) to fully normal state (8.7 K). (e) Susceptibility image of (d), taken simultaneously.

transition, the sample becomes highly nonhomogeneous and the behavior is governed by the disorder. Figure 4 follows part of a network as it is driven through the superconducting transition. In the presence of a fixed applied current, we increase the temperature in small steps through T_c, and map the current density for each arrested temperature. The transition between the two well-organized behaviors shown in Fig. 2 involves dramatic changes in the spatial distribution of the current flow. The evolution process is summarized in the following:

(a) Superconductivity is destroyed in isolated sections of the network, as depicted by the susceptibility map (e). This leads to some vertical flow as the supercurrents bypass resistive areas, see (b)–(d).

(b) As more sections turn normal, large portions of the network do not carry current, while the system is still globally superconducting (negligible voltage), see (f)–(l). At this stage the dominant player is the disordered distribution of local T_c, which overshadows the effect of Meissner screening on the overall current distribution. The current is no longer concentrated on the edges, but rather exhibits a typical percolative flow.

(c) When there is no percolative superconducting path across the network, resistive parts carry current and the voltage increases. Gradually the current distribution becomes homogeneously spread (m)–(p).

The simultaneous measurements of current flow and susceptibility demonstrate the difference between maps of conductance and the maps of current flow. The current bypasses regions of the network, which are strongly superconducting, but are not part of the percolation backbone. This is illustrated in Fig. 5, which shows the $S(x,y)$ and $|\vec{J}(x,y)|$ at the same region of the network.

In addition, in this regime of network collapse, the specific details of current injection dramatically affect the network current map. The mixture of normal and superconducting sections opens a number of possible low dissipation paths depending on the entry point to the network. This is demonstrated in Fig. 5(c), which shows the current map of sample S1 (Nb on glass) where superconductivity in the lead is also widely inhomogeneous. Clear correlation between the homogeneity of the flow in the pad and the network is observed.

IV. CONCLUSIONS

In conclusion, we visualize the way the current flows in a superconducting network. We find that, at the various stages of the superconductor-normal transition, the current favors different spatial-flow configurations, which are all nonuniform. Our findings have relevance for a number of applications. The results presented here should be considered when designing superconducting circuits, as different parts of the circuit may be dominant depending

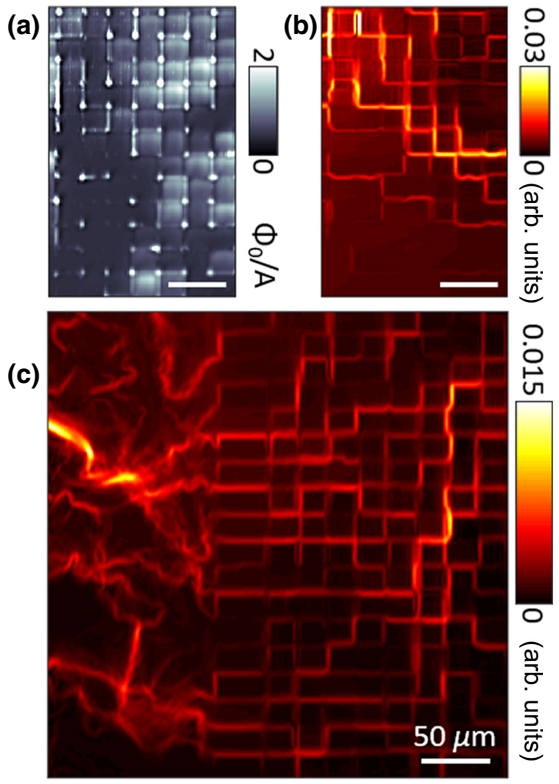

FIG. 5. Susceptibility image (a) and $|\vec{J}(x,y)|$ map (b) of sample S1 near its superconducting transition (8.3 K). (c) The current flow in the lead, where it is injected into network (sample S1, 8.3 K).

on the operation conditions, and the way the current is injected into the circuit. This is especially relevant these days, for the design of quantum circuits based on Josephson-junction arrays [31], disordered superconductors, and superconducting qubit assemblies. Another implication can be for the recent effort to create and study coupled resistance networks [32–35]. For a system of coupled superconducting networks, since we use an ac technique to image the currents we can excite each network at a different frequency and thus image the local currents in each network individually and simultaneously.

ACKNOWLEDGMENTS

We thank Michael Stern for assistance in sample preparation. X.W. and B.K. are supported by the European Research Council Grant No. ERC-2019-COG-866236, the Israeli Science Foundation, Grant No. ISF-1251/19, COST Action CA16218, and the QuantERA Project No. 731473. M.L., I.V., and A.F. are supported by the Israel Science Foundation, Grant No. ISF-783/17.

[1] J. Clarke and F. K. Wilhelm, Superconducting quantum bits, Nature **453**, 1031 (2008).

[2] C. H. van der Wal, A. C. J. ter Haar, F. K. Wilhelm, R. N. Schouten, C. J. P. M. Harmans, T. P. Orlando, S. Lloyd, and J. E. Mooij, Quantum superposition of macroscopic persistent-current states, Science **290**, 773 (2000).

[3] T. Duty, D. Gunnarsson, K. Bladh, and P. Delsing, Coherent dynamics of a josephson charge qubit, Phys. Rev. B **69**, 140503 (2004).

[4] K. B. Cooper, M. Steffen, R. McDermott, R. W. Simmonds, S. Oh, D. A. Hite, D. P. Pappas, and J. M. Martinis, Observation of Quantum Oscillations between a Josephson Phase Qubit and a Microscopic Resonator Using Fast Readout, Phys. Rev. Lett. **93**, 180401 (2004).

[5] C. Song, K. Xu, H. Li, Y.-R. Zhang, X. Zhang, W. Liu, Q. Guo, Z. Wang, W. Ren, J. Hao, H. Feng, H. Fan, D. Zheng, D.-W. Wang, H. Wang, and S.-Y. Zhu, Generation of multicomponent atomic schrödinger cat states of up to 20 qubits, Science **365**, 574 (2019).

[6] J. Kirtley, M. Ketchen, K. Stawiasz, J. Sun, W. Gallagher, S. Blanton, and S. Wind, High-resolution scanning squid microscope, Appl. Phys. Lett. **66**, 1138 (1995).

[7] F. Wellstood, Y. Gim, A. Amar, R. Black, and A. Mathai, Magnetic microscopy using squids, IEEE Trans. Appl. Supercond. **7**, 3134 (1997).

[8] S. Chatraphorn, E. F. Fleet, F. C. Wellstood, L. A. Knauss, and T. M. Eiles, Scanning SQUID microscopy of integrated circuits, Appl. Phys. Lett. **76**, 2304 (2000).

[9] E. Šimánek, Origin of the resistivity minima in granular superconductors, Phys. Rev. B **25**, 237 (1982).

[10] L. de Arcangelis, S. Redner, and A. Coniglio, Multiscaling approach in random resistor and random superconducting networks, Phys. Rev. B **34**, 4656 (1986).

[11] M. P. Fisher, Quantum Phase Slips and Superconductivity in Granular Films, Phys. Rev. Lett. **57**, 885 (1986).

[12] D. C. Wright, D. J. Bergman, and Y. Kantor, Resistance fluctuations in random resistor networks above and below the percolation threshold, Phys. Rev. B **33**, 396 (1986).

[13] Y. M. Strelniker, A. Frydman, and S. Havlin, Percolation model for the superconductor-insulator transition in granular films, Phys. Rev. B **76**, 224528 (2007).

[14] P. Martinoli and C. Leemann, Two dimensional Josephson junction arrays, J. Low Temp. Phys. **118**, 699 (2000).

[15] L. Ponta, A. Carbone, M. Gilli, and P. Mazzetti, Resistive transition in granular disordered high T_c superconductors: A numerical study, Phys. Rev. B **79**, 134513 (2009).

[16] L. Ponta, V. Andreoli, and A. Carbone, Superconducting-insulator transition in disordered Josephson junctions networks, Eur. Phys. J. B **86**, 24 (2013).

[17] R. Panghotra, B. Raes, C. C. de Souza Silva, I. Cools, W. Keijers, J. Scheerder, V. Moshchalkov, and J. Van de Vondel, Giant fractional Shapiro steps in anisotropic Josephson junction arrays, Commun. Phys. **3**, 1 (2020).

[18] B. W. Gardner, J. C. Wynn, P. G. Björnsson, E. W. J. Straver, K. A. Moler, J. R. Kirtley, and M. B. Ketchen, Scanning superconducting quantum interference device susceptometry, Rev. Sci. Instrum. **72**, 2361 (2001).

[19] M. E. Huber, N. C. Koshnick, H. Bluhm, L. J. Archuleta, T. Azua, P. G. Björnsson, B. W. Gardner, S. T. Halloran, E. A. Lucero, and K. A. Moler, Gradiometric micro-SQUID susceptometer for scanning measurements of mesoscopic samples, Rev. Sci. Instrum. **79**, 053704 (2008).

[20] Y. Shperber, N. Vardi, E. Persky, S. Wissberg, M. E. Huber, and B. Kalisky, Scanning squid microscopy in a cryogen-free cooler, Rev. Sci. Instrum. **90**, 053702 (2019).

[21] J. R. Kirtley, B. Kalisky, J. A. Bert, C. Bell, M. Kim, Y. Hikita, H. Y. Hwang, J. H. Ngai, Y. Segal, F. J. Walker, C. H. Ahn, and K. A. Moler, Scanning SQUID susceptometry of a paramagnetic superconductor, Phys. Rev. B **85**, 224518 (2012).

[22] A. Kremen, H. Khan, Y. L. Loh, T. I. Baturina, N. Trivedi, A. Frydman, and B. Kalisky, Imaging quantum fluctuations near criticality, Nat. Phys. **14**, 1205 (2018).

[23] B. J. Roth, N. G. Sepulveda, and J. P. Wikswo Jr, Using a magnetometer to image a two-dimensional current distribution, J. Appl. Phys. **65**, 361 (1989).

[24] E. Persky, N. Vardi, A. M. R. V. L. Monteiro, T. C. van Thiel, H. Yoon, Y. Xie, B. Fauqué, A. D. Caviglia, H. Y. Hwang, K. Behnia, J. Ruhman, and B. Kalisky, Non-universal current flow near the metal-insulator transition in an oxide interface, Nat. Commun. **12**, 3311 (2021).

[25] F. Tafuri, J. R. Kirtley, P. G. Medaglia, P. Orgiani, and G. Balestrino, Magnetic Imaging of Pearl Vortices in Artificially Layered $(Ba_{0.9}Nd_{0.1}CuO_{2+x})_m/(CaCuO_2)_n$ Systems, Phys. Rev. Lett. **92**, 157006 (2004).

[26] S. Wissberg, A. Frydman, and B. Kalisky, Local view of superconducting fluctuations, Appl. Phys. Lett. **112**, 262602 (2018).

[27] J. M. Martinis, S. Nam, J. Aumentado, and C. Urbina, Rabi Oscillations in a Large Josephson-Junction Qubit, Phys. Rev. Lett. **89**, 117901 (2002).

[28] M. H. Devoret, J. M. Martinis, and J. Clarke, Measurements of Macroscopic Quantum Tunneling out of the Zero-Voltage State of a Current-Biased Josephson Junction, Phys. Rev. Lett. **55**, 1908 (1985).

[29] R. F. Voss and R. A. Webb, Macroscopic Quantum Tunneling in 1-μm Nb Josephson Junctions, Phys. Rev. Lett. **47**, 265 (1981).

[30] M. Grajcar, A. Izmalkov, E. Il'ichev, T. Wagner, N. Oukhanski, U. Hübner, T. May, I. Zhilyaev, H. E. Hoenig, Y. S. Greenberg, V. I. Shnyrkov, D. Born, W. Krech, H.-G. Meyer, A. Maassen van den Brink, and M. H. S. Amin, Low-frequency measurement of the tunneling amplitude in a flux qubit, Phys. Rev. B **69**, 060501 (2004).

[31] M. Galin, F. Rudau, E. Borodianskyi, V. Kurin, D. Koelle, R. Kleiner, V. Krasnov, and A. Klushin, Direct Visualization of Phase-Locking of Large Josephson Junction Arrays by Surface Electromagnetic Waves, Phys. Rev. Appl. **14**, 024051 (2020).

[32] S. V. Buldyrev, R. Parshani, G. Paul, H. E. Stanley, and S. Havlin, Catastrophic cascade of failures in interdependent networks, Nature **464**, 1025 (2010).

[33] M. M. Danziger, A. Bashan, and S. Havlin, Interdependent resistor networks with process-based dependency, New J. Phys. **17**, 043046 (2015).

[34] M. M. Danziger, O. I. Moskalenko, S. A. Kurkin, X. Zhang, S. Havlin, and S. Boccaletti, Explosive synchronization coexists with classical synchronization in the Kuramoto model, Chaos: An Interdisciplinary J. Nonlinear Sci. **26**, 065307 (2016).

[35] M. Laav *et al.*, Interdependent superconducting networks, (unpublished).